

Article

Iron-Doped Titanium Dioxide Nanoparticles As Potential Scaffold for Hydrazine Chemical Sensor Applications

Ahmad Umar ^{1,2,*}, Farid A. Harraz ^{2,3}, Ahmed A. Ibrahim ^{1,2}, Tubia Almas ^{1,2,4}, Rajesh Kumar ⁵, M. S. Al-Assiri ^{2,6} and Sotirios Baskoutas ⁴ 

¹ Department of Chemistry, Faculty of Science and Arts, Najran University, Najran-11001, Saudi Arabia; ahmedragal@yahoo.com (A.A.I.); tubiaalmas@gmail.com (T.A.)

² Promising Centre for Sensors and Electronic Devices (PCSED), Najran University, Najran-11001, Saudi Arabia; fharraz.68@yahoo.com (F.A.H.); msassiri@gmail.com (M.S.A.-A.)

³ Nanostructured Materials and Nanotechnology Division, Central Metallurgical Research and Development Institute (CMRDI), P.O. Box: 87 Helwan, Cairo 11421, Egypt

⁴ Department of Materials Science, University of Patras, GR-26504 Patras, Greece; bask@upatras.gr

⁵ Department of Chemistry, Jagdish Chandra DAV College, Dasuya-144205, India; rk.ash2k7@gmail.com

⁶ Department of Physics, Faculty of Science and Arts, Najran University, Najran-11001, Saudi Arabia

* Correspondence: umahmad@nu.edu.sa or ahmadumar786@gmail.com

Received: 5 January 2020; Accepted: 13 February 2020; Published: 17 February 2020



Abstract: Herein, we report the fabrication of a modified glassy carbon electrode (GCE) with high-performance hydrazine sensor based on Fe-doped TiO₂ nanoparticles prepared via a facile and low-cost hydrothermal method. The structural morphology, crystalline, crystallite size, vibrational and scattering properties were examined through different characterization techniques, including FESEM, XRD, FTIR, UV–Vis, Raman and photoluminescence spectroscopy. FESEM analysis revealed the high-density synthesis of Fe-doped TiO₂ nanoparticles with the average diameter of 25 ± 5 nm. The average crystallite size of the synthesized nanoparticles was found to be around 14 nm. As-fabricated hydrazine chemical sensors exhibited 1.44 μA μM⁻¹ cm⁻² and 0.236 μM sensitivity and limit of detection (LOD), respectively. Linear dynamic ranged from 0.2 to 30 μM concentrations. Furthermore, the Fe-doped TiO₂ modified GCE showed a negligible inference behavior towards ascorbic acid, uric acid, glucose, SO₄²⁻, NO₃⁻, Pb²⁺ and Ca²⁺ ions on the hydrazine sensing performance. Thus, Fe-doped TiO₂ modified GCE can be efficiently used as an economical, easy to fabricate and selective sensing of hydrazine and its derivatives.

Keywords: Fe-doped TiO₂; hydrothermal; GCE; hydrazine; chemical sensor; amperometry

1. Introduction

Hydrazine is extensively used in rocket propellants, pesticides, explosives, photography chemicals, antioxidants and plant growth regulators in various related industries and laboratories [1,2]. Effluents released from these industries and laboratories are the foremost environmental source of hydrazine. It is considered one of the poisonous chemicals even at low concentration and is very hazardous to living organisms. The potential symptoms of hydrazine exposure range from eye and nose irritation, pulmonary edema, skin dermatitis, temporary blindness and serious damage to many human organs such as the kidney and liver [3–5]. Due to its mutagenic and carcinogenic behavior, it has been cited in the Environmental Protection Agency (EPA) list. It is therefore mandatory to trace the presence of minor amounts of hydrazine in the aqueous medium.

Previously reported techniques for the detection of hydrazine include spectrophotometry [6], fluorimetry [7,8], chemiluminescence [9] and potentiometry [10,11]. However, all these methods are accompanied by several disadvantages like low sensitivity, and they require expensive instrumentation followed by complicated procedures. Electrochemical determination is considered to be the promising alternative for the determination of hydrazine in terms of selectivity, sensitivity and portability, with an economical and simple operating procedure [12,13]. Unfortunately, hydrazine undergoes direct oxidation at the bare electrode surface, thus resulting in sluggish electrode kinetics and high over potentials [14,15]. Therefore, chemically modified electrodes have been used to detect hydrazine, which significantly reduce the overpotential, as well as accelerate redox reactions and hence the oxidation current responses [16,17].

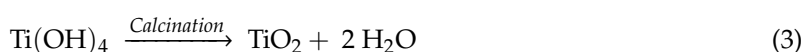
Recently, there is a big interest in the utilization of new materials in scientific societies due to improved processibility, applicability and vast applications in various fields of sciences. In the past few years, tremendous work has been done on metal oxide based nanomaterials or composites, especially ZnO [18], CuO [19,20], TiO₂ [21,22] and MnO₂ [23], which are considered an ideal platform for material preparation used in pharmaceuticals and cosmetics industries, for the treatment of wastewater and in other fields [24]. TiO₂ is one of the most extensively used semiconductor materials owing to its non-toxicity, high performance, great stability and low preparation cost. Due to its good conductivity, high electrocatalytic activity and electron transport properties, TiO₂ is the most suitable material for devising the electrodes for various electrochemical and biosensing applications. Khodari et al. [25] used an electrochemical sensor, prepared by casting TiO₂ nanoparticles (NPs) onto a carbon electrode surface, for the determination of resorcinol. The TiO₂ NPs were demonstrated to be competent in boosting the electron transfer between resorcinol and the electrode surface as well as transport of resorcinol molecules to the surface of the sensor. Guo and coworkers [26,27] synthesized TiO₂ nanofibers for the bio-sensing of glucose. The fabricated TiO₂ nanofibers exhibited good direct electrochemistry as well as magnificent sensitivity along with fast response time for the detection of glucose. In order to further increase the electron transfer rate between the working modified electrode and the analyte solution and, hence, rapid and sensitive current response, doping of metal oxides has been reported as one of the best ways. Among the various dopants, Fe³⁺ ions are most suitable owing to their similar ionic radii to that of Ti⁴⁺ ions. Fe³⁺ ions (63 pm) can easily replace the Ti⁴⁺ ions (68 pm) from the TiO₂ crystal lattice. Further, Fe³⁺ ions prevent electron-hole (e⁻-h⁺) recombination, better charge separation and incorporation of oxygen vacancies in the crystal lattice and surface of the TiO₂ [28,29]. Additionally, the choice of Fe³⁺ ions as dopant has also been confirmed for some other semiconductor metal oxides. Hexamethylenediamine (HMDA) grafted and Fe nanoparticles incorporation into SnO₂ nanostructures exhibited strong surface affinity of 8.5 μmol/m² for H₂, as an important aspect of green energy storage applications at ambient temperature and pressure conditions [30]. ZnO powders doped with Fe nanoparticles through an in situ dispersion method showed improved conductivity and capacitance as compared to undoped ZnO nanoparticles [31]. HMDA grafted and Fe nanoparticles doped ZnO nanoparticles showed excellent conductivity which was attributed to the formation of effective proton-conductivity on the surface of the ZnO as well as proton transfer between Fe nanoparticles [32]. Fe-doped TiO₂ nanoparticles displayed superior photocatalytic degradation of methylene blue dye, phenol and toxic organic compounds as compared to undoped TiO₂ under UV and visible light illumination [33–35].

Herein, Fe-doped TiO₂ nanoparticles were prepared through a facile hydrothermal technique and subsequently analyzed using different characterization techniques for their various characteristics and to affirm the formation of the doped TiO₂ nanoparticles. Modified glassy carbon electrode (GCE) was fabricated by coating a thin film of Fe-doped TiO₂ nanoparticles onto it. As-fabricated hydrazine chemical sensors exhibited excellent hydrazine chemical sensing parameters.

2. Experimental Details

2.1. Synthesis of Fe-Doped TiO₂ Nanoparticles

For the preparation of Fe-doped TiO₂ nanoparticle, a facile hydrothermal method was adopted (2% doping of Fe ion was performed in the Fe-doped TiO₂ nanoparticle). Tetrabutyl titanate (Ti(BuO)₄) and ferric nitrate (Fe(NO₃)₃) were used as TiO₂ precursor and Fe dopant, respectively. Twenty milliliters of 0.5 M Ti(BuO)₄ solution was poured drop-wise to 5 M aqueous NaOH solution followed by the addition of 20 mL of 0.1 M Fe(NO₃)₃ solution dropwise. A Teflon lined stainless steel autoclave containing above solution was then heated at 200 °C for 10 h. The following reaction mechanisms have been proposed for the synthesis of Fe-doped TiO₂ nanoparticles (Equations (1)–(3)).



During the hydrothermal process, tetrabutyl titanate was hydrolyzed to titanium hydroxide (Ti(OH)₄) and sodium butoxide. Ferric nitrate used as dopant was also hydrolyzed to its hydroxide, i.e., ferric hydroxide (Fe(OH)₃). BuONa and NaNO₃ were removed by washing with ethanol and deionized (DI) water. These washings also eliminated any unreacted Fe(NO₃)₃. Thoroughly washed Ti(OH)₄ and Fe(OH)₃ were dried for 6 h in an electric oven at 70 °C. During calcination, titanium hydroxide was converted into TiO₂ with Fe³⁺ ions occupying the lattice sites in the TiO₂ crystal lattice. The calcination was carried out in oxygen atmosphere at 450 °C for 2 h. The calculated synthesis yield of the synthesized Fe-doped TiO₂ nanoparticles were found to be 0.8 g.

2.2. Characterizations of Fe-Doped TiO₂ Nanoparticles

X-ray diffraction (XRD; PAN analytical Xpert Pro. Cambridge, UK) with Cu–Kα radiation was performed for the analysis of crystal phase and crystallite size. The optical characteristics were estimated by using UV–Vis Spectrophotometer (Perkin Elmer-Lambda 950, Waltham, MA, USA) within the wavelength range of 200–800 nm by dispersing and sonicating the Fe-doped TiO₂ in distilled water for 30 min. Scattering properties of the doped TiO₂ material were analyzed by Raman spectrum and examined using Raman spectrometer (Perkin Elmer-FTIR Spectrum-100, Waltham, MA, USA) from 100 to 900 cm^{−1}. FTIR spectrum of the Fe-doped TiO₂ was collected by FTIR spectrophotometer (Perkin Elmer-FTIR Spectrum-100, Waltham, MA, USA) through KBr pelletization from 500 to 4000 cm^{−1}. The photoelectronic properties of the Fe-doped TiO₂ nanoparticles were analyzed through photoluminescence spectral measurement.

2.3. Hydrazine Chemical Sensor Fabrication

Prior to electrode coating with Fe-doped TiO₂ nanoparticles, the GCE with surface area of 0.071 cm² (Bio-Logic SAS, Seyssinet-Pariset, France) was polished with a 1 μm polishing diamond. After this, the surface of the GCE was further polished with 0.05 μm alumina slurry and finally washed with distilled water. The modified GCEs with active materials (Fe-doped TiO₂) were fabricated as follows: The GCE surface was smoothly coated by the Fe-doped TiO₂ using ethyl acetate and conducting binder–butyl carbitol acetate followed by drying at 60 °C for 3 h. A three electrode electrochemical cell was connected to electrochemical workstation, Zahner Zennium, Germany, with a Pt wire as a counter electrode, and Fe-doped TiO₂ nanoparticle modified GCE as working electrode and an Ag/AgCl (saturated KCl) as a reference electrode were used during the electrochemical measurements. Different concentrations of hydrazine (0.2 μM–30 μM) were electrochemically tested. All the electroanalytical experiments were performed in 0.1 M phosphate buffer solution (PBS) of pH 7.4 at room temperature.

3. Results and Discussion

3.1. Characterizations and Properties of Fe-Doped TiO₂ Nanoparticles

Figure 1 depicts the XRD diffraction patterns of Fe-doped-TiO₂ nanoparticles. The XRD studies clearly demonstrated the presence of both anatase and rutile phases with anatase as the major phase. The presence of main diffraction peaks in the XRD pattern of Fe-doped-TiO₂ nanoparticles at $2\theta = 25.28, 37.8, 48.07, 54.25$ and $62.63, 68.9, 70.28$ and 75.13 were consistent with (101), (103), (004), (200), (105), (211), (204), (116), (220) and (107) lattice planes of anatase phase (JCPDS No. 21-1272) [24].

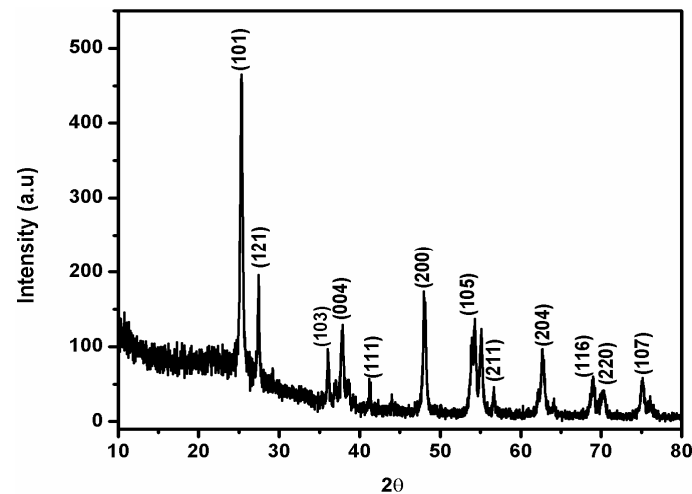


Figure 1. XRD pattern of Fe-doped TiO₂ nanoparticles.

The XRD peaks corresponding to rutile phase also emerged at $2\theta = 27.50$ and 41.54 diffraction angles corresponding to (121) and (111) diffraction planes (JCPDS No. 21-1276). The synthesized samples did not exhibit any diffraction peaks for Fe, which suggests that the Fe³⁺ content in the Fe-doped TiO₂ was below the detection limit, and due to almost similar ionic radii, the Fe³⁺ ions could substitute Ti⁴⁺ from some of the lattice sites of TiO₂ as discussed earlier. This further indicates that Fe³⁺ ions were successfully integrated into TiO₂ matrix homogeneously without the development of iron oxide on the TiO₂ surface. This homogeneous distribution of Fe³⁺ ions in TiO₂ matrix and low concentration, responsible for the absence of any Fe³⁺ peaks in the XRD patterns, have also been reported earlier in the literature [36,37]. The average crystallite size of the synthesized nanoparticles was estimated using the Scherrer formula (Equation (4)) and was found to be around 14 nm.

$$d = \frac{0.89\lambda}{\beta \cos \theta} \quad (4)$$

where $\lambda = 1.542 \text{ \AA}$, $\theta =$ Bragg angle of diffraction, $\beta =$ full width at half maximum.

The detailed structural and morphological properties of Fe-doped TiO₂ were examined by FESEM analysis. The corresponding low and high magnification FESEM images are depicted in Figure 2a–d. A large number of spherical shaped and highly agglomerated Fe-doped TiO₂ particles with an average diameter of about 20 nm can be seen. In addition to spherical shapes, some Fe-doped TiO₂ with cubic, pentagonal, oval and other irregular geometries can also be seen from high magnification FESEM images (Figure 2c,d).

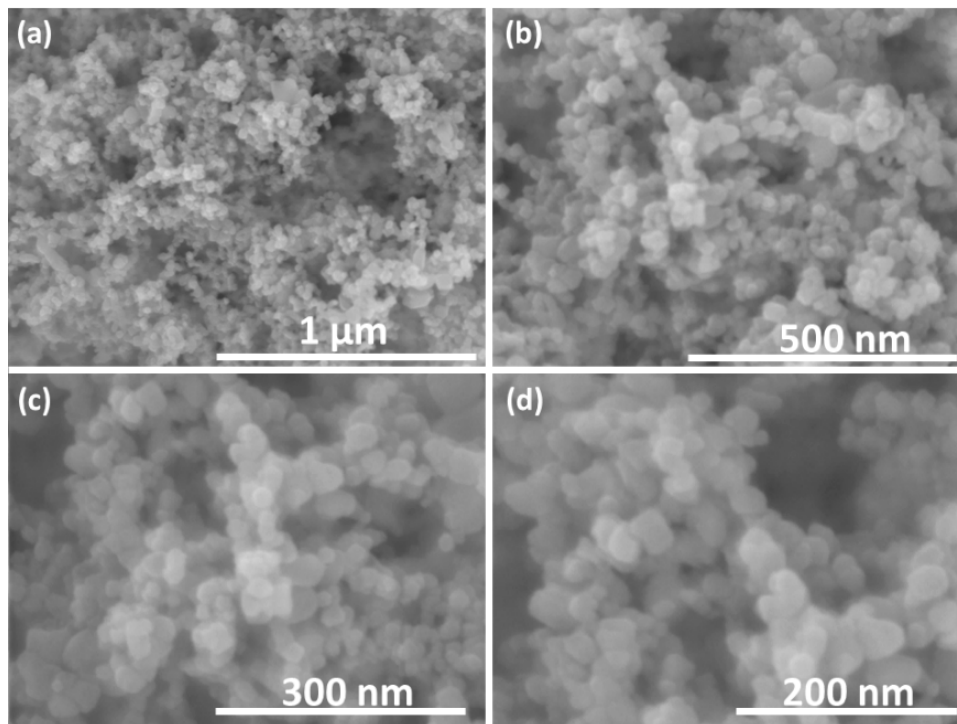


Figure 2. (a) and (b) Low magnification and (c) and (d) high magnification FESEM images for Fe-doped TiO₂ nanoparticles.

To observe the optical properties of the Fe-doped TiO₂ nanoparticles, a UV–Vis absorption spectroscopic study was performed. It can be examined from Figure 3a that Fe-doped TiO₂ nanoparticles exhibited a wide absorption peak below 400 nm, which is the typical absorption of TiO₂. This peak can be attributed to the electronic excitation from lower energy level to higher energy level in the anatase phase of the TiO₂. Furthermore, the change in color of the sample from white (pure TiO₂) to creamish yellow (Fe-doped TiO₂) depicted the increase in absorption towards visible light due to the incorporation of dopant metal [38].

Figure 3b illustrates the Raman spectra of Fe-doped TiO₂ nanoparticles. Five main bands—144.2, 195, 396.4, 513.2 and 634.8 cm^{−1}, corresponding to the six Raman active modes—were illustrated for the anatase phase of TiO₂ (3E_g, 2B_{1g} and 1A_{2g}) [39]. The spectra indicated the crystalline nature of the synthesized nanoparticles. Furthermore, no additional peak related to the iron oxide was seen, which corroborates the results of XRD.

Figure 3c shows the FTIR spectra of Fe-doped TiO₂ nanoparticles. The spectrum reflects that doping had no effect on the bonding environment of the TiO₂ host nanoparticles. The broadband at 3433 cm^{−1} was assigned to the symmetric and asymmetric stretching vibrations of O–H bonds of the adsorbed water molecules during sample formation. An additional peak at 1628 cm^{−1} was attributed to the bending vibration related to the hydroxyl group of the adsorbed water. The band centered at ~520 cm^{−1} was due to metal–oxygen, i.e., Ti–O and Fe–O, bonds [40].

The photoelectronic properties of Fe-doped TiO₂ nanoparticles were studied from the photoluminescence spectrum (Figure 3d). The UV region peak at around 375 nm is likely related to the near-band-edge (NBE) excitonic emission. Interestingly, the energy corresponding to above NBE peak is close to the energy gap of 3.17 eV of anatase TiO₂ as reported earlier [40]. The NBE transition originated from the electrons–holes recombination. The incorporation of dopant Fe did not cause any significant alteration in the PL spectrum.

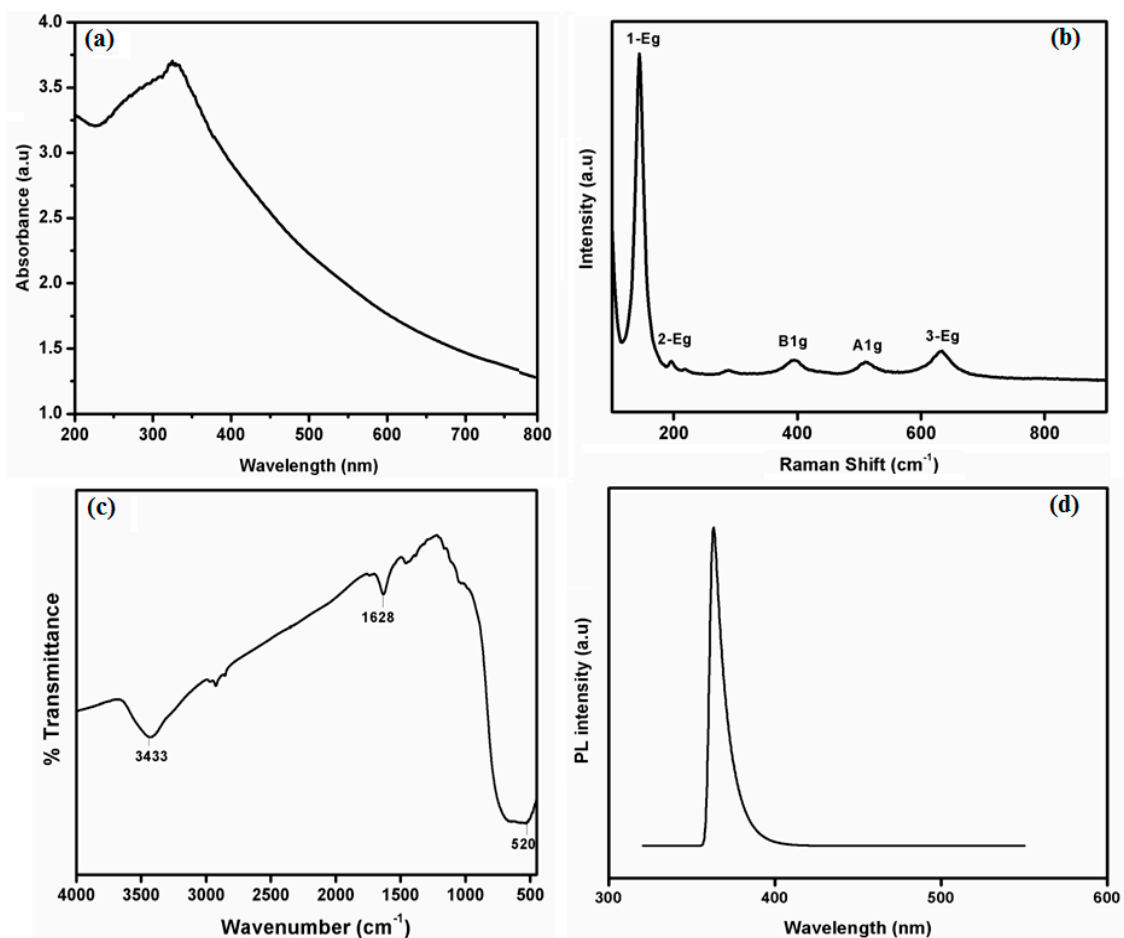


Figure 3. (a) UV-Vis absorption spectrum, (b) room temperature Raman spectrum, (c) FTIR and (d) PL spectrum of Fe-doped TiO₂ nanoparticles.

3.2. Electrochemical Sensing Properties of Hydrazine Using Fe-Doped TiO₂ Nanoparticles

The electrochemical sensing capability of Fe-doped TiO₂ nanostructure was examined using cyclic voltammetry. Figure 4a,b shows typical cyclic voltammogram (CV) of bare GCE, undoped TiO₂ modified GCE and Fe-doped TiO₂ modified GCE in absence and presence, respectively, of 0.5 mM hydrazine in 0.1 M PBS (pH 7.4) at 50 mVs⁻¹ scan rate. As can be observed from Figure 4a, in blank PBS solution bare GCE, undoped TiO₂ modified GCE, and Fe-doped TiO₂ modified GCE did not generate any characteristic peak in the selected voltage range. However, with the addition of 0.5 mM hydrazine, no significant peak was observed by bare electrode, but a significant oxidation peak at 0.45 V vs. Ag/AgCl was detected in the case of both undoped TiO₂ modified GCE and Fe-doped TiO₂ modified electrode (Figure 4b), which clearly illustrated the efficient electrocatalytic activity of the modified GCE. The current response at Fe-doped TiO₂ modified electrode was much larger than the undoped TiO₂ modified GCE, ~137% larger, which indicates the enhanced electrocatalytic activity of coated GCE after the addition of Fe.

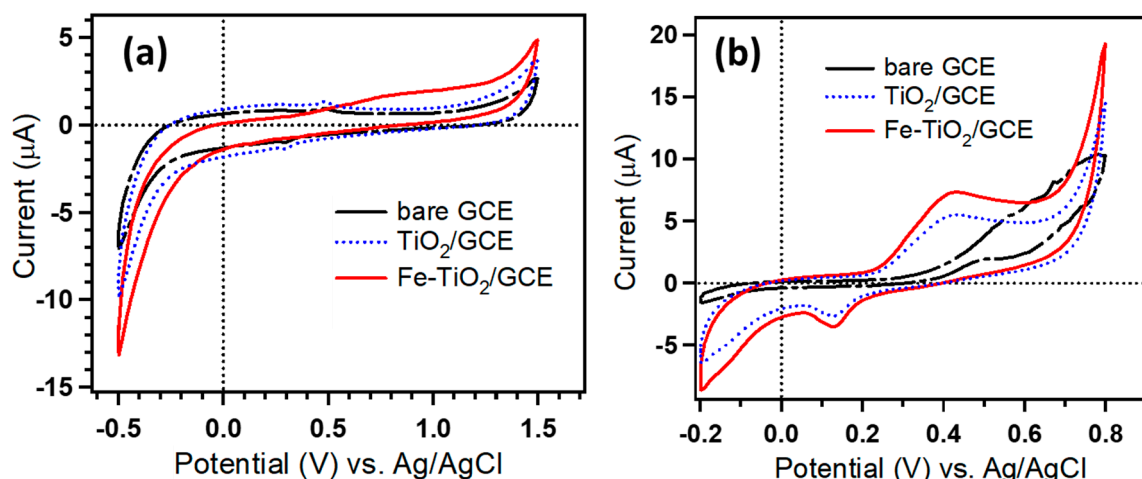


Figure 4. Cyclic voltammograms measured at 50 mVs^{-1} in 0.1 M phosphate buffer solution (PBS) (pH 7.4) (a) with absence of hydrazine and (b) in presence of 0.5 mM hydrazine using bare glassy carbon electrode (GCE), TiO_2 modified GCE and Fe-doped TiO_2 modified GCE.

3.3. Amperometric Studies

The amperometric (i - t) response was also carried out with the purpose to detect the hydrazine analyte using Fe-doped TiO_2 nanoparticle modified GCE. Amperometric studies were performed, and the constant potential was set at a value of 0.45 V with successive addition of hydrazine (0.2 – $30 \text{ }\mu\text{M}$) into a continuously stirred 0.1 M PBS (pH 7.4). As revealed in Figure 5a, Fe-doped TiO_2 modified GCE fabricated sensor illustrated a significant and steep rise in the current value after each successive addition of hydrazine. The measured current increased rapidly with a response time of $\sim 20 \text{ s}$ during the amperometric measurements. The corresponding calibration curve for amperometric hydrazine sensing showed a linear response in the concentration range 0.2 to $30 \text{ }\mu\text{M}$ (Figure 5b). The correlation coefficient of the line R^2 was found to be 0.998 , and the linear equation was $y = 0.1019x + 0.0157$. The linearity in the plot also confirmed that the hydrazine oxidation process was diffusion-controlled and indicated the fast electron transfer rate, which led to the sharper and well-defined peaks.

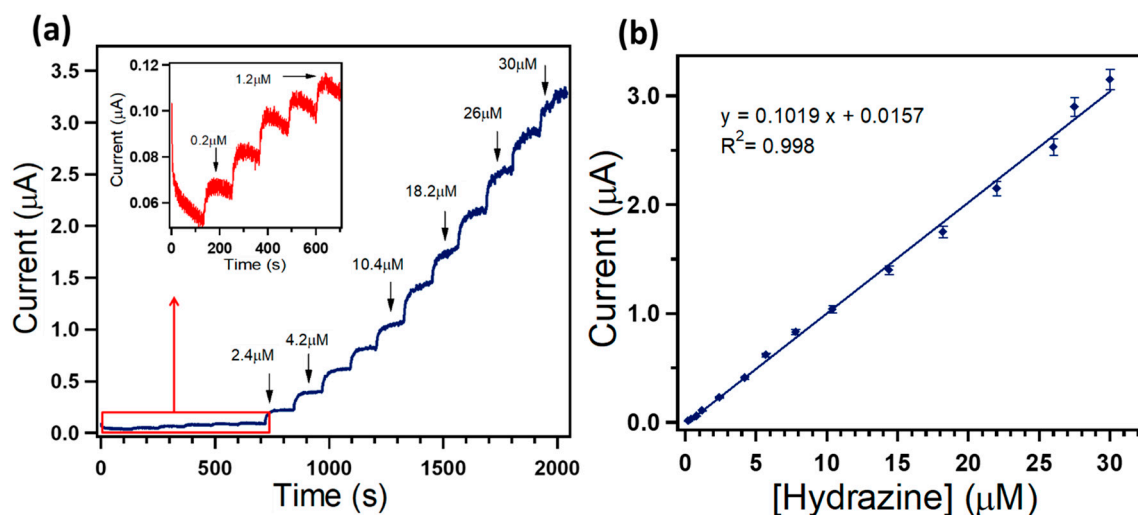
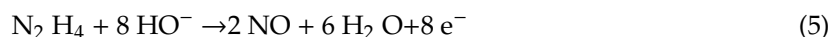


Figure 5. (a) Current–time (i - t) response of Fe-doped TiO_2 modified GCE for 0.2 – $30 \text{ }\mu\text{M}$ hydrazine concentrations at a constant potential $+0.45 \text{ V}$ vs. Ag/AgCl . Inset shows an enlarged part of the early stage addition (0.2 – $1.2 \text{ }\mu\text{M}$). (b) The corresponding current–concentration calibration graph.

It has been proposed that hydrazine in slightly basic medium (pH = 7.4) is oxidized onto the surface of the Fe-doped TiO₂ to release electrons (Equation (5)) [41,42].



The schematic proposed hydrazine sensing by Fe-doped TiO₂ is shown in Figure 6.

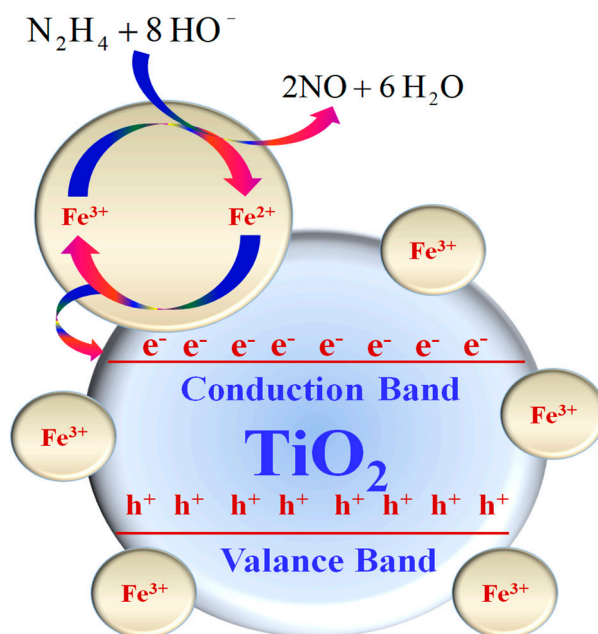
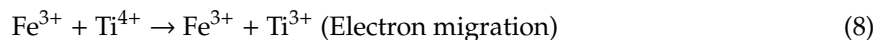


Figure 6. Proposed mechanism for the hydrazine sensing by Fe-doped TiO₂ nanoparticles.

The redox behavior of the Fe³⁺ ions facilitate the transfer of electrons released from the oxidation of the hydrazine to the conduction band of the TiO₂ or migrate the electrons to reduce the Ti⁴⁺ to Ti³⁺ ions. Li et al. [43] proposed that Fe³⁺ can act as a hole as well as an electron trap, which further enhances the electron transfer process. Furthermore, Zhu et al. [44] proposed the following reactions to depict the redox nature of Fe³⁺ ions ((Equations (6)–(9)).



Therefore, when hydrazine comes in contact with Fe-doped TiO₂, the electron density in the conduction band increases, which leads to the increase in electrical conductivity and, thus, increase in the current potential. The higher the concentration of the hydrazine, the greater is the electron density in the conduction band and, hence, the current potential is higher.

The sensitivity of the synthesized sensor was calculated from the slope of the calibration curve divided by the electrode area [45,46]. The limit of detection (LOD) of the fabricated hydrazine sensor was accordingly estimated via the following equation (Equation (10)):

$$\text{LOD} = 3.0 \cdot \sigma_B / b \quad (10)$$

where σ_B is the standard deviation of the population of the blank signals (0.008 μA) and b is the slope of the regression line. It is possible to replace σ_B by the residual standard deviation of the regression,

$s_{y/x}$, also known as standard error of the regression [47]. The sensitivity and LOD were found to be $1.44 \mu\text{A } \mu\text{M}^{-1} \text{cm}^{-2}$ and $0.236 \mu\text{M}$, respectively. These obtained results demonstrated the potential of the Fe-doped TiO_2 nanostructure modified electrode as a suitable electrochemical sensor for sensitive and selective determination of hydrazine. The synthesized hydrazine electrochemical sensor was reliable and depicted fantastic reproducibility. It was ascertained that no significant decrease in sensitivity was observed when tested for more than three weeks while being stored at room temperature in a closed container.

In order to assess the analytical potential of the fabricated sensor for real sample analysis, the selectivity of Fe-doped TiO_2 nanostructures to hydrazine was evaluated. The selectivity test of the sensor was conducted to check the influence of some interfering electro-active chemical species on the sensing property of Fe-doped TiO_2 by measuring the i - t response. Figure 7 demonstrates the amperometric responses of Fe-doped TiO_2 modified GCE for the successive addition of different concentrations of hydrazine and $100 \mu\text{M}$ of ascorbic acid (AA), uric acid (UA), glucose, SO_4^{2-} , NO_3^- , Pb^{2+} and Ca^{2+} at a regular interval of 100 s in 0.1 M PBS at an applied potential value of +0.45 V. The negligible change in the observed current, even if the various co-existing interfering species were present, undoubtedly revealed the excellent selectivity of the fabricated sensor.

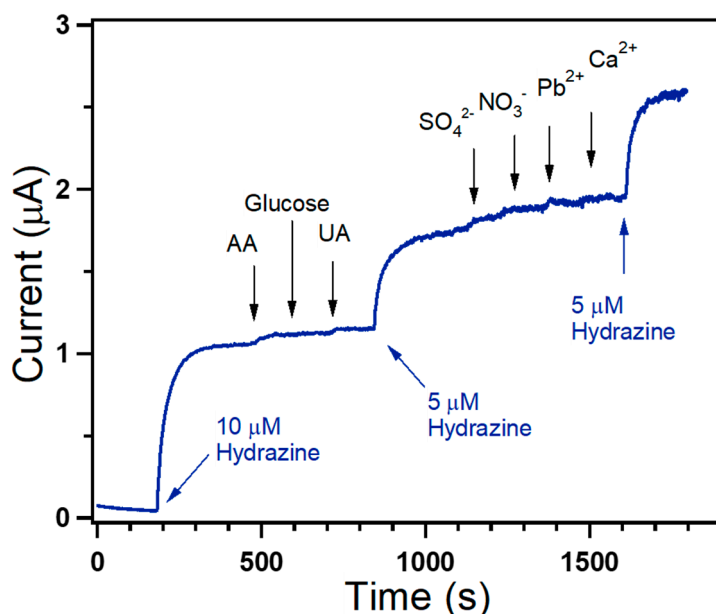


Figure 7. Amperometric (i - t) measurement showing the interference behavior of the Fe-doped TiO_2 coated GCE upon the successive injections of 10 or $5 \mu\text{M}$ hydrazine and each $100 \mu\text{M}$ of AA, glucose, UA, SO_4^{2-} , NO_3^- , Pb^{2+} and Ca^{2+} into a continuously stirred 0.1 M PBS (pH 7.4) solution operating at +0.45 V vs. Ag/AgCl.

The sensor parameters of Fe-doped TiO_2 nanoparticle modified GCE and other recently reported sensors are compared in Table 1. Detailed comparison shows that the fabricated sensor had excellent electrocatalytic performance for selective detection and sensing of hydrazine.

Table 1. Comparison of the sensor parameters of the Fe-doped TiO₂ coated GCE sensor with some recently reported hydrazine electrochemical sensor materials.

Sensor Electrode	Sensitivity	LOD	Ref.
Leaf shape CuO/OMC/GCE	0.00487 $\mu\text{A} \cdot \mu\text{M}^{-1} \cdot \text{cm}^{-2}$	0.887 μM	[4]
NiCo ₂ S ₄ sphere/GCE	179.1 $\mu\text{A} \cdot \text{mM}^{-1} \cdot \text{cm}^{-2}$	0.6 μM	[5]
WO ₃ NPs/Au electrode	0.185 $\mu\text{A} \cdot \mu\text{M}^{-1} \cdot \text{cm}^{-2}$	144.73 μM	[32]
Polythiophene/ZnO/GCE	1.22 $\mu\text{A} \cdot \mu\text{M}^{-1} \cdot \text{cm}^{-2}$	0.207 μM	[48]
Ag@Fe ₃ O ₄ nanosphere/GCE	270.0 $\mu\text{A} \cdot \text{mM}^{-1} \cdot \text{cm}^{-2}$	0.06 μM	[49]
CdO/CNT nanocomposites/GCE	25.79 $\mu\text{A} \cdot \mu\text{M}^{-1} \cdot \text{cm}^{-2}$	4.0 pM	[50]
Pd/Co-NCNTs	343.9 $\mu\text{A} \cdot \text{mM}^{-1} \cdot \text{cm}^{-2}$	0.007 μM	[51]
Pd (CNT-Pd)/GCE	0.3 $\mu\text{A} \cdot \text{mM}^{-1} \cdot \text{cm}^{-2}$	8.0 μM	[52]
Nanoporous gold/ITO	0.161 $\mu\text{A} \cdot \mu\text{M}^{-1} \cdot \text{cm}^{-2}$	0.0043 μM	[53]
α -Fe ₂ O ₃ /polyaniline nanocomposite	1.93 $\text{mA} \cdot \mu\text{M}^{-1} \cdot \text{cm}^{-2}$	0.153 μM	[54]
Chrysanthemum-like Co ₃ O ₄ /GCE	107.9 $\mu\text{A} \cdot \text{mM}^{-1} \cdot \text{cm}^{-2}$	3.7 μM	[55]
AuNPs/CNTs-rGO/GCE	9.73 $\mu\text{A} \cdot \mu\text{M}^{-1} \cdot \text{cm}^{-2}$	0.065 μM	[56]
Fe-doped TiO ₂ NPs/GCE	1.44 $\mu\text{A} \cdot \mu\text{M}^{-1} \cdot \text{cm}^{-2}$	0.236 μM	This work

4. Conclusions

In summary, highly crystalline Fe-doped TiO₂ nanoparticles were synthesized through hydrothermal synthesis and subsequently characterized by different characterization techniques. Finally, Fe-doped TiO₂ nanoparticles were applied as an efficient electron mediator for the fabrication of hydrazine chemical sensor using GCE. As-fabricated modified GCE showed sensitivity, LOD and LDR of 1.44 $\mu\text{A} \mu\text{M}^{-1} \text{cm}^{-2}$, 0.236 μM and 0.2–30 μM , respectively, through an amperometric sensing approach. It was proposed that redox behavior of the Fe³⁺ ions facilitates the transfer of electrons released from the oxidation of the hydrazine to the conduction band of the TiO₂, which leads to the increase in electrical conductivity. The negligible change in the observed current in the presence of various co-existing interfering chemical species further confirms the excellent selectivity of the fabricated sensor towards hydrazine.

Author Contributions: A.U., F.A.H., A.A.I., T.A., R.K., M.S.A.-A. and S.B. conceived of the presented idea and developed and performed the experiments. All of the authors discussed the results and contributed to the final manuscript. All authors have read and agreed to the published version of the manuscript.

Funding: This research was funded by the Ministry of Education, Kingdom of Saudi Arabia through a grant (PCSED-013-18) under the Promising Centre for Sensors and Electronic Devices (PCSED) at Najran University, Kingdom of Saudi Arabia.

Acknowledgments: Authors would like to acknowledge the support of the Ministry of Education, Kingdom of Saudi Arabia for this research through a grant (PCSED-013-18) under the Promising Centre for Sensors and Electronic Devices (PCSED) at Najran University, Kingdom of Saudi Arabia.

Conflicts of Interest: The authors declare no conflict of interest.

References

1. Wahab, R.; Ahmad, N.; Alam, M.; Ahmed, J. Nanorods of ZnO: An effective hydrazine sensor and their chemical properties. *Vacuum* **2019**, *165*, 290–296. [[CrossRef](#)]
2. Guo, S.-H.; Guo, Z.-Q.; Wang, C.-Y.; Shen, Y.; Zhu, W.-H. An ultrasensitive fluorescent probe for hydrazine detection and its application in water samples and living cells. *Tetrahedron* **2019**, *75*, 2642–2646. [[CrossRef](#)]
3. Nemakal, M.; Aralekallu, S.; Mohammed, I.; Swamy, S.; Sannegowda, L.K. Electropolymerized octabenzimidazole phthalocyanine as an amperometric sensor for hydrazine. *J. Electroanal. Chem.* **2019**, *839*, 238–246. [[CrossRef](#)]
4. Wang, L.; Meng, T.; Jia, H.; Feng, Y.; Gong, T.; Wang, H.; Zhang, Y. Electrochemical study of hydrazine oxidation by leaf-shaped copper oxide loaded on highly ordered mesoporous carbon composite. *J. Colloid Interface Sci.* **2019**, *549*, 98–104. [[CrossRef](#)]

5. Duan, C.; Dong, Y.; Sheng, Q.; Zheng, J. A high-performance non-enzymatic electrochemical hydrazine sensor based on NiCo₂S₄ porous sphere. *Talanta* **2019**, *198*, 23–29. [[CrossRef](#)]
6. George, M.; Nagaraja, K.S.; Balasubramanian, N. Spectrophotometric determination of hydrazine. *Talanta* **2008**, *75*, 27–31. [[CrossRef](#)]
7. Rios, A.; Silva, M.; Valcarcel, M. Fluorimetric determination of ammonia, hydrazine and hydroxylamine and their mixtures by differential kinetic methods. *Fresenius' Zeitschrift Für Anal. Chem.* **1985**, *320*, 762–768. [[CrossRef](#)]
8. Collins, G.E.; Rose-Pehrsson, S.L. Sensitive, fluorescent detection of hydrazine via derivatization with 2,3-naphthalene dicarboxaldehyde. *Anal. Chim. Acta* **1993**, *284*, 207–215. [[CrossRef](#)]
9. Collins, G.E.; Lattur, S.; Rose-Pehrsson, S.L. Chemiluminescence detection of hydrazine vapor. *Talanta* **1995**, *42*, 543–551. [[CrossRef](#)]
10. Bravo, P.; Isaacs, F.; Ramírez, G.; Azócar, I.; Trollund, E.; Aguirre, M.J. A potentiometric hydrazine sensor: Para-Ni-tetraaminophenylporphyrin/Co-cobaltite/SNO₂:F modified electrode. *J. Coord. Chem.* **2007**, *60*, 2499–2507. [[CrossRef](#)]
11. Ganesh, S.; Khan, F.; Ahmed, M.K.; Pandey, S.K. Potentiometric determination of free acidity in presence of hydrolysable ions and a sequential determination of hydrazine. *Talanta* **2011**, *85*, 958–963. [[CrossRef](#)] [[PubMed](#)]
12. Kannan, P.K.; Moshkalev, S.A.; Rout, C.S. Electrochemical sensing of hydrazine using multilayer graphene nanobelts. *RSC Adv.* **2016**, *6*, 11329–11334. [[CrossRef](#)]
13. Rostami, S.; Azizi, S.N.; Ghasemi, S. Simultaneous electrochemical determination of hydrazine and hydroxylamine by CuO doped in ZSM-5 nanoparticles as a new amperometric sensor. *New J. Chem.* **2017**, *41*, 13712–13723. [[CrossRef](#)]
14. Jena, B.K.; Raj, C.R. Ultrasensitive nanostructured platform for the electrochemical sensing of hydrazine. *J. Phys. Chem. C* **2007**, *111*, 6228–6232. [[CrossRef](#)]
15. Deng, J.; Deng, S.; Liu, Y. Highly sensitive electrochemical sensing platform for hydrazine detection. *Int. J. Electrochem. Sci.* **2018**, *13*, 3566–3574. [[CrossRef](#)]
16. Gu, X.; Li, X.; Wu, S.; Shi, J.; Jiang, G.; Jiang, G.; Tian, S. A sensitive hydrazine hydrate sensor based on a mercaptomethyl-terminated trinuclear Ni(II) complex modified gold electrode. *RSC Adv.* **2016**, *6*, 8070–8078. [[CrossRef](#)]
17. Wang, J.; Wang, H.; Yang, S.; Tian, H.; Liu, Y.; Hao, Y.; Zhang, J.; Sun, B. A Fluorescent Probe for Sensitive Detection of Hydrazine and Its Application in Red Wine and Water. *Anal. Sci.* **2018**, *34*, 329–333. [[CrossRef](#)]
18. Yang, Y.J. Electrodeposition of ZnO Nanofibers for Sensitive Determination of Hydrazine and Nitrite. *Sens. Lett.* **2017**, *14*, 1187–1192. [[CrossRef](#)]
19. Ma, Y.; Li, H.; Wang, R.; Wang, H.; Lv, W.; Ji, S. Ultrathin willow-like CuO nanoflakes as an efficient catalyst for electro-oxidation of hydrazine. *J. Power Sources* **2015**, *289*, 22–25. [[CrossRef](#)]
20. Wang, G.; Gu, A.; Wang, W.; Wei, Y.; Wu, J.; Wang, G.; Zhang, X.; Fang, B. Copper oxide nanoarray based on the substrate of Cu applied for the chemical sensor of hydrazine detection. *Electrochem. Commun.* **2009**, *11*, 631–634. [[CrossRef](#)]
21. Wang, G.; Zhang, C.; He, X.; Li, Z.; Zhang, X.; Wang, L.; Fang, B. Detection of hydrazine based on Nano-Au deposited on Porous-TiO₂ film. *Electrochim. Acta* **2010**, *55*, 7204–7210. [[CrossRef](#)]
22. Yi, Q.; Niu, F.; Yu, W. Pd-modified TiO₂ electrode for electrochemical oxidation of hydrazine, formaldehyde and glucose. *Thin Solid Films* **2011**, *519*, 3155–3161. [[CrossRef](#)]
23. Wu, J.; Zhou, T.; Wang, Q.; Umar, A. Morphology and chemical composition dependent synthesis and electrochemical properties of MnO₂-based nanostructures for efficient hydrazine detection. *Sens. Actuators B Chem.* **2016**, *224*, 878–884. [[CrossRef](#)]
24. Shirsath, S.R.; Pinjari, D.V.; Gogate, P.R.; Sonawane, S.H.; Pandit, A.B. Ultrasound assisted synthesis of doped TiO₂ nano-particles: Characterization and comparison of effectiveness for photocatalytic oxidation of dyestuff effluent. *Ultrason. Sonochem.* **2013**, *20*, 277–286. [[CrossRef](#)]
25. Khodari, M.; Mersal, G.A.M.; Rabie, E.M.; Assaf, H.F. Electrochemical sensor based on carbon paste electrode modified by TiO₂ nano-particles for the voltammetric determination of resorcinol. *Int. J. Electrochem. Sci.* **2018**, *13*, 3460–3474. [[CrossRef](#)]
26. Guo, Q.; Zhang, M.; Li, X.; Li, X.; Li, H.; Lu, Y.; Song, X.; Wang, L. A novel CuO/TiO₂ hollow nanofiber film for non-enzymatic glucose sensing. *RSC Adv.* **2016**, *6*, 99969–99976. [[CrossRef](#)]

27. Guo, Q.; Liu, L.; Zhang, M.; Hou, H.; Song, Y.; Wang, H.; Zhong, B.; Wang, L. Hierarchically mesostructured porous TiO₂ hollow nanofibers for high performance glucose biosensing. *Biosens. Bioelectron.* **2017**, *92*, 654–660. [[CrossRef](#)]
28. Spriano, S.; Yamaguchi, S.; Baino, F.; Ferraris, S. A critical review of multifunctional titanium surfaces: New frontiers for improving osseointegration and host response, avoiding bacteria contamination. *Acta Biomater.* **2018**, *79*, 1–22. [[CrossRef](#)]
29. Zhang, Y.; Cheng, K.; Lv, F.; Huang, H.; Fei, B.; He, Y.; Ye, Z.; Shen, B. Photocatalytic treatment of 2,4,6-trinitrotoluene in red water by multi-doped TiO₂ with enhanced visible light photocatalytic activity. *Colloids Surf. A Physicochem. Eng. Asp.* **2014**, *452*, 103–108. [[CrossRef](#)]
30. Bouazizi, N.; Bargougui, R.; Boudharaa, T.; Khelil, M.; Benghnia, A.; Labiadh, L.; Slama, R.B.; Chaouachi, B.; Ammar, S.; Azzouz, A. Synthesis and characterization of SnO₂-HMD-Fe materials with improved electric properties and affinity towards hydrogen. *Ceram. Int.* **2016**, *42*, 9413–9418. [[CrossRef](#)]
31. Bouazizi, N.; Ajala, F.; Khelil, M.; Lachheb, H.; Khirouni, K.; Houas, A.; Azzouz, A. Zinc oxide incorporating iron nanoparticles with improved conductance and capacitance properties. *J. Mater. Sci. Mater. Electron.* **2016**, *27*, 11168–11175. [[CrossRef](#)]
32. Bouazizi, N.; Ajala, F.; Bettaibi, A.; Khelil, M.; Benghnia, A.; Bargougui, R.; Louhichi, S.; Labiadh, L.; Slama, R.B.; Chaouachi, B.; et al. Metal-organo-zinc oxide materials: Investigation on the structural, optical and electrical properties. *J. Alloys Compd.* **2016**, *656*, 146–153. [[CrossRef](#)]
33. Khan, M.A.M.; Siwach, R.; Kumar, S.; Alhazaa, A.N. Role of Fe doping in tuning photocatalytic and photoelectrochemical properties of TiO₂ for photodegradation of methylene blue. *Opt. Laser Technol.* **2019**, *118*, 170–178. [[CrossRef](#)]
34. Moradi, V.; Ahmed, F.; Jun, M.B.G.; Blackburn, A.; Herring, R.A. Acid-treated Fe-doped TiO₂ as a high performance photocatalyst used for degradation of phenol under visible light irradiation. *J. Environ. Sci. China* **2019**, *83*, 183–194. [[CrossRef](#)]
35. Sood, S.; Umar, A.; Mehta, S.K.; Kansal, S.K. Highly effective Fe-doped TiO₂ nanoparticles photocatalysts for visible-light driven photocatalytic degradation of toxic organic compounds. *J. Colloid Interface Sci.* **2015**, *450*, 213–223. [[CrossRef](#)]
36. Ismael, M. Enhanced photocatalytic hydrogen production and degradation of organic pollutants from Fe (III) doped TiO₂ nanoparticles. *J. Environ. Chem. Eng.* **2020**, *8*, 103676. [[CrossRef](#)]
37. Khan, M.A.; Woo, S.I.; Yang, O.B. Hydrothermally stabilized Fe(III) doped titania active under visible light for water splitting reaction. *Int. J. Hydrogen Energy* **2008**, *33*, 5345–5351. [[CrossRef](#)]
38. Niu, Y.; Xing, M.; Zhang, J.; Tian, B. Visible light activated sulfur and iron co-doped TiO₂ photocatalyst for the photocatalytic degradation of phenol. *Catal. Today* **2013**, *201*, 159–166. [[CrossRef](#)]
39. Ali, I.; Kim, S.-R.; Park, K.; Kim, J.-O. One-step electrochemical synthesis of graphene oxide-TiO₂ nanotubes for improved visible light activity. *Opt. Mater. Express* **2017**, *7*, 1535. [[CrossRef](#)]
40. Prajapati, B.; Kumar, S.; Kumar, M.; Chatterjee, S.; Ghosh, A.K. Investigation of the physical properties of Fe:TiO₂ -diluted magnetic semiconductor nanoparticles. *J. Mater. Chem. C* **2017**, *5*, 4257–4267. [[CrossRef](#)]
41. Dong, B.; He, B.L.; Huang, J.; Gao, G.Y.; Yang, Z.; Li, H.L. High dispersion and electrocatalytic activity of Pd/titanium dioxide nanotubes catalysts for hydrazine oxidation. *J. Power Sources* **2008**, *175*, 266–271. [[CrossRef](#)]
42. Shukla, S.; Chaudhary, S.; Umar, A.; Chaudhary, G.R.; Mehta, S.K. Tungsten oxide (WO₃) nanoparticles as scaffold for the fabrication of hydrazine chemical sensor. *Sens. Actuators B Chem.* **2014**, *196*, 231–237. [[CrossRef](#)]
43. Li, Z.; Shen, W.; He, W.; Zu, X. Effect of Fe-doped TiO₂ nanoparticle derived from modified hydrothermal process on the photocatalytic degradation performance on methylene blue. *J. Hazard. Mater.* **2008**, *155*, 590–594. [[CrossRef](#)]
44. Zhu, J.; Zheng, W.; He, B.; Zhang, J.; Anpo, M. Characterization of Fe-TiO₂ photocatalysts synthesized by hydrothermal method and their photocatalytic reactivity for photodegradation of XRG dye diluted in water. *J. Mol. Catal. A Chem.* **2004**, *216*, 35–43. [[CrossRef](#)]
45. Dong, B.; Chai, Y.M.; Liu, Y.Q.; Liu, C.G. Facile Synthesis and High Activity of Novel Ag/TiO₂-NTs Composites for Hydrazine Oxidation. *Adv. Mater. Res.* **2011**, *197*, 1073–1078. [[CrossRef](#)]
46. Dong, B.; He, B.L.; Chai, Y.M.; Liu, C.G. Novel Pt nanoclusters/titanium dioxide nanotubes composites for hydrazine oxidation. *Mater. Chem. Phys.* **2010**, *120*, 404–408. [[CrossRef](#)]

47. Miller, J.N.; Miller, J.N. *Statistics and Chemometrics for Analytical Chemistry*, 5th ed.; Pearson Prentice Hall: Edinburgh, Scotland, 2005.
48. Faisal, M.; Harraz, F.A.; Al-Salami, A.E.; Al-Sayari, S.A.; Al-Hajry, A.; Al-Assiri, M.S. Polythiophene/ZnO nanocomposite-modified glassy carbon electrode as efficient electrochemical hydrazine sensor. *Mater. Chem. Phys.* **2018**, *214*, 126–134. [[CrossRef](#)]
49. Dong, Y.; Yang, Z.; Sheng, Q.; Zheng, J. Solvothermal synthesis of Ag@Fe₃O₄ nanosphere and its application as hydrazine sensor. *Colloids Surf. A Physicochem. Eng. Asp.* **2018**, *538*, 371–377. [[CrossRef](#)]
50. Rahman, M.M.; Alam, M.M.; Alamry, K.A. Sensitive and selective m-tolyl hydrazine chemical sensor development based on CdO nanomaterial decorated multi-walled carbon nanotubes. *J. Ind. Eng. Chem.* **2019**, *77*, 309–316. [[CrossRef](#)]
51. Zhang, Y.; Huang, B.; Ye, J.; Ye, J. A sensitive and selective amperometric hydrazine sensor based on palladium nanoparticles loaded on cobalt-wrapped nitrogen-doped carbon nanotubes. *J. Electroanal. Chem.* **2017**, *801*, 215–223. [[CrossRef](#)]
52. Gioia, D.; Casella, I.G. Pulsed electrodeposition of palladium nano-particles on coated multi-walled carbon nanotubes/naion composite substrates: Electrocatalytic oxidation of hydrazine and propranolol in acid conditions. *Sens. Actuators B Chem.* **2016**, *237*, 400–407. [[CrossRef](#)]
53. Tang, Y.-Y.; Kao, C.-L.; Chen, P.-Y. Electrochemical detection of hydrazine using a highly sensitive nanoporous gold electrode. *Anal. Chim. Acta* **2012**, *711*, 32–39. [[CrossRef](#)] [[PubMed](#)]
54. Harraz, F.A.; Ismail, A.A.; Al-Sayari, S.A.; Al-Hajry, A.; Al-Assiri, M.S. Highly sensitive amperometric hydrazine sensor based on novel α -Fe₂O₃/crosslinked polyaniline nanocomposite modified glassy carbon electrode. *Sens. Actuators B Chem.* **2016**, *234*, 573–582. [[CrossRef](#)]
55. Zhou, T.; Lu, P.; Zhang, Z.; Wang, Q.; Umar, A. Perforated Co₃O₄ nanoneedles assembled in chrysanthemum-like Co₃O₄ structures for ultra-high sensitive hydrazine chemical sensor. *Sens. Actuators B Chem.* **2016**, *235*, 457–465. [[CrossRef](#)]
56. Zhao, Z.; Sun, Y.; Li, P.; Zhang, W.; Lian, K.; Hu, J.; Chen, Y. Preparation and characterization of AuNPs/CNTs-ErGO electrochemical sensors for highly sensitive detection of hydrazine. *Talanta* **2016**, *158*, 283–291. [[CrossRef](#)]



© 2020 by the authors. Licensee MDPI, Basel, Switzerland. This article is an open access article distributed under the terms and conditions of the Creative Commons Attribution (CC BY) license (<http://creativecommons.org/licenses/by/4.0/>).